AIAA SciTech Forum
8–12 January 2018, Kissimmee, Florida
2018 Wind Energy Symposium

10.2514/6.2018-0753

Interaction of small scale Homogenenous Isotropic Turbulence with an Actuator Disk

Aditya Ghate*, Niranjan Ghaisas†, Aaron Towne‡ and Sanjiva Lele§

The interaction of a dragging, fixed thrust coefficient actuator disk with decaying homogeneous isotropic turbulence (HIT) of varying spatial integral length scales and dissipation rates is studied using Large Eddy Simulation performed at high resolution. Modulation of the turbulence pressure, the deformation of the inflow turbulence as it enters the core, and the wake shear layer turbulence are characterized in detail, and various turbulence quantities pertinent for modeling the problem are reported. The shear layer entrainment (and hence wake recovery) is shown to be strongly sensitive to the *integral length scale* of the upstream HIT (as opposed to its *intensity*), and this observation is reconciled using a space-time modal decomposition of the flow field to identify the dominant Kelvin-Helmholtz wavepackets that dictate the shear layer growth rate.

I. Introduction

Actuator disk formulations for bluff body interactions with turbulence have been abundantly used in simulations involving propellers[1, 2], helicopter rotors[3, 4] and wind turbines [5, 6]. A primary reason for the popularity of actuator disk (AD) formulations in the wind energy community is that AD formulations generate reasonable surrogates for real wind turbine wakes at a much smaller cost as compared to other blade-resolved methods. Several large eddy simulation studies employing AD parameterizations [5, 6] have shown that the mean, time-averaged features of the flow can be reproduced accurately, for model wind turbines subjected to well-controlled inflow conditions [7], as well as for real wind turbines subjected to the atmospheric boundary layer [8]. Numerous models of varying sophistication, ranging from parabolized thin-shear RANS models [9, 10] to simple analytical formulations [11–14], have been developed for the time-averaged characteristics of the wakes.

In contrast, the state of turbulence within the wakes has received limited attention in numerical simulations as well as modeling studies. Most LES tend to focus on macro-scale phenomena such as the vertical flux of the mean kinetic energy in the context of atmospheric stability or layout optimization[15–18], and as such the simulations do not have sufficient grid resolution to robustly characterize the multiscale nature of wake shear turbulence. Furthermore, while a few studies (e.g. Quarton & Ainslie (1990)[19], Crespo & Hernandez (1996)[20], Xie & Archer (2016)[21]) have developed and evaluated empirical models for the *wake-added* streamwise turbulence intensity, other aspects of the wake turbulence, such as how wake turbulence affects the overall anisotropy and the integral length scales, have not been considered. Recent LES [22] have also suggested that streamwise turbulence intensity alone is not sufficient to characterize the effect of the ABL on wind turbine wakes.

Stochastic models that rely on the principle of enrichment of either the larger (resolved) scales or the mean flow with smaller scales have enabled very efficient simulations of ABL turbulence. Examples of such models include the one by Mann [23], the TurbSim model [24, 25], and the Gabor mode- based kinematic simulation (KS) approach [26]. The limited understanding of the turbulence in wind turbine wakes has precluded development of such enrichment-based reduced order models for this problem. An improved understanding of the interaction between ambient ABL turbulence and the shear-generated turbulence in turbine wakes is critical for this purpose. As a step towards this goal, a simpler problem is considered in this paper, that of the interaction of an AD momentum sink subjected to a uniform inflow with superimposed and homogeneous isotropic turbulence whose properties are varied in the simulations. Recent work by Martinéz Tossas (2017)[27] also considered the problem of decaying HIT incident on an actuator line parameterization for a wind turbine (with an integral scale larger than the turbine diameter), however the focus of that work was on studying the sensitivity to choice of the subgrid scale model used in the LES. The purpose of this paper is to provide a

*PhD Candidate, Dept. of Aeronautics & Astronautics, Stanford University, and AIAA student member.
†Postdoctoral fellow, Center for Turbulence Research, Stanford University.
‡Postdoctoral fellow, Center for Turbulence Research, Stanford University.
§Professor, Dept. of Aeronautics & Astronautics, and Dept. of Mechanical Engineering, Stanford University, and AIAA associate member.

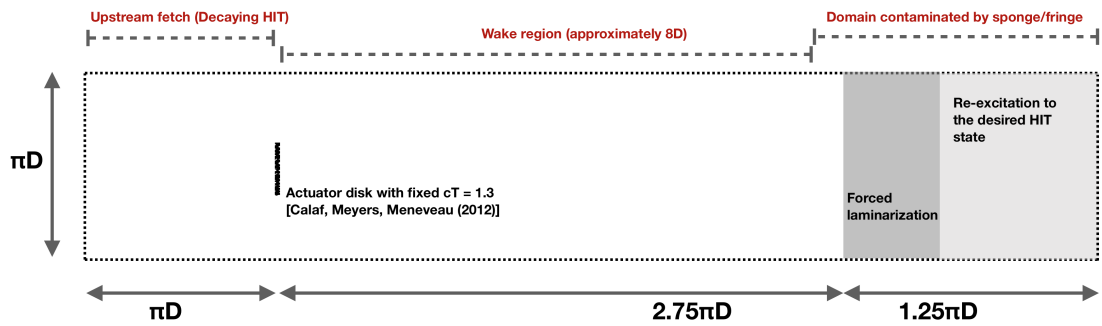

Fig. 1 Problem configuration. All lengths are non-dimensionalized using the actuator disk diameter, D

detailed characterization of the AD wake turbulence, and to distinguish its character from that of the incident ambient turbulence.

The problem setup including the properties of the inflow turbulence, and the resulting mean flow features are described in Section II. The wake recovery as deduced using wake shear layer growth is found to be strongly affected by the integral length scale of the inflow turbulence, and only weakly sensitive to the dissipation rate (or the *intensity*). Section III focuses on the characterization of the multi-scale features of the wake turbulence. In particular, the anisotropy associated with different scales, and the pressure fields are analyzed, and it is shown that the flow field downstream of an AD can be split into three distinct regions, namely, the wake core, the shear layer, and the external flow. In Section IV we re-analyse the wake turbulence using a frequency domain form of Proper Orthogonal Decomposition (POD) originally proposed by Lumley (1970)[28], and recently revisited by Towne et. al. (2017)[29] (referred to as *Spectral POD*, henceforth) to explain the sensitivity of shear layer growth (and hence wake recovery) to the incident turbulence characteristics. Section V concludes the paper with a brief summary of findings and implications of the present study.

II. Simulation details and the mean flow

A. Problem setup

The problem configuration is illustrated in Figure 1. A concurrent forced HIT simulation in a $2\pi^3$ domain is bandpass filtered to a desired state which is forced within the *fringe region* (see Nordström et. al. 1999 [30]) of the simulation domain. The sponge upstream of the fringe region is used to damp the turbulent wake to a laminar uniform flow base state prior to enriching the flow with the HIT. While the use of two separate sponge/fringe regions increases the simulation domain length, it alleviates the restrictive CFL constraints of using a single fringe region. The presence of the fringe forcing contaminates the domain upstream of the fringe region due to non-locality of the induced pressure field. However, this contaminated region can easily be identified (as discussed in Section 4), and all simulations presented in this paper have an effective domain of approximately 8 AD diameters downstream from the actuator disk, where the flow is unaffected by the sponge/fringe region.

All simulations correspond to an actuator disk with a constant thrust coefficient ($c_T = 1.3$) with the regularization method introduced by Calaf, Meyers & Meneveau (2010)[17]. The concurrent HIT simulation used to force the inflow to a desired state, uses external forcing in Fourier space at wavenumber shells of specified radius ($1.5 \leq |\boldsymbol{k}| \leq 2.5$), which sets the dissipation rate for the turbulent energy cascade. Since the simulation is performed in the vanishing limit of molecular viscosity ($\mathrm{Re} \rightarrow \infty$), the *Sigma* model developed by Nicoud et al. [31] is used to provide subgrid scale closure. Incompressible, filtered Navier stokes equations are solved in the rotational form, and spatial differentiation is performed using Fourier collocation in all three directions. Since the simulation eliminates aliasing errors using $2/3rd$ rule which is interpreted as filtering using a projection operator, the LES formulation can be consistently interpreted as *explicitly filtered LES* in the classical sense. Time stepping is performed using the strong stability preserving variant of 4th order accurate Runge Kutta scheme[32]. All the results shown in this paper use a numerical mesh of $1280 \times 256 \times 256$ grid points which corresponds to a grid spacing of approximately 0.012D. The concurrent forced HIT uses $256 \times 256 \times 256$ grid points with the same grid spacing as the primary simulation. All the simulations are performed at a fixed CFL

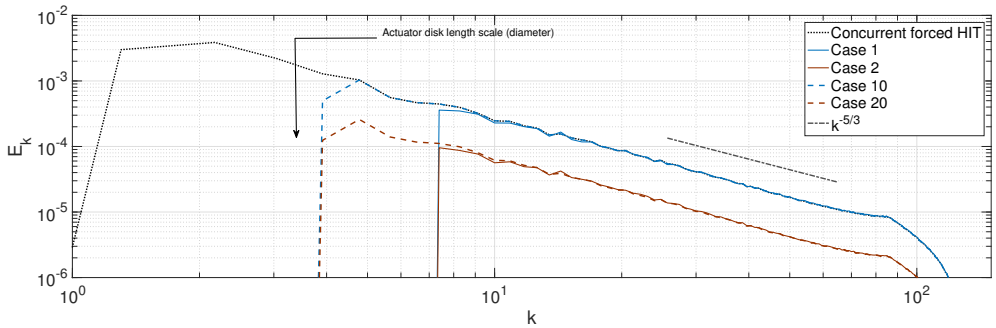

Fig. 2 Energy spectra for the 4 different inflow states simulated, along with the concurrent forced HIT.

Table 1 Properties for the 4 different inflow states simulated.

HIT case description	Rel. L_0	Rel. ε	Rel. decay time scale, τ	Turb. Intensity (at incidence)
Case 1 (Small L_0, Large ε)	1	1	1	3.75%
Case 2 (Small L_0, Small ε)	1	0.125	2	2.5%
Case 10 (Large L_0, Large ε)	1.75	1	1.45	5.0%
Case 20 (Large L_0, Small ε)	1.75	0.125	2.90	3.25%

number of 0.8. Finally note that the periodicity assumption in the vertical (z) and spanwise (y) directions, introduces a substantial blocking effect on the flow; however this is not particularly pertinent in the present context since our focus in this paper is primarily on wake turbulence rather than the evolution of the far-wake.

B. Inflow properties

The inflow is tailored to the desired state by appropriate bandpass filtering of a concurrent forced HIT. This leads to 2 free parameters (in the inviscid limit) that set the inflow HIT: a) an Integral length scale, L_0 and b) the dissipation rate, ε. Table 1 summarizes the 4 different inflow states simulated and Figure 2 shows their respective energy spectra. Note that for all cases studied, the integral length scale of the incident turbulence is kept smaller than actuator disk diameter. This ensures that the turbulent wake does not meander due to interactions with large scale ambient turbulence, and the length scales and turbulence intensities being studied are not very dissimilar to observations in the atmospheric boundary layer (ABL) under stably stratified conditions*.

It is further important to acknowledge that the isotropic turbulence that enters the domain, decays before impinging on the actuator disk at the relative time scales reported in Table 1. At incidence, Case 20 (large length scale, low dissipation rate) and Case 1 (small length scale, large dissipation rate) have a very similar measure of turbulence intensity, however these states are achieved differently in the two cases.

C. The mean flow and wake recovery

The mean (time averaged) flow streamlines, the contours of the Frobenius norm of the mean velocity gradient tensor, and dU/dx contours are shows in Figure 3(a-c). These contours help identify region where significant distortion of the inflow turbulence is expected due to mean velocity gradients. It is evident that the HIT ingested by the actuator disk will undergo expansion due to the slowdown in the freestream caused by the actuator disk. However, when we look at the frobenius norm of the mean velocity gradient tensor, it is clear that the gradients in the shear layer overwhelm the expansion expected at the centerline. Hence we expect three distinct regions in the simulated domain: a) the decaying isotropic turbulence upstream of the AD, b) the axisymmetrically expanded, anisotropic turbulence within the core region immediately downstream of the AD, and c) the shear layer turbulence generated due to the shear layer instability which is triggered by a finite amplitude perturbation caused by the incident HIT.

*ABL turbulence is however, not isotropic. The strong velocity and potential temperature gradients result in a highly damped wall normal component for turbulent fluctuations.

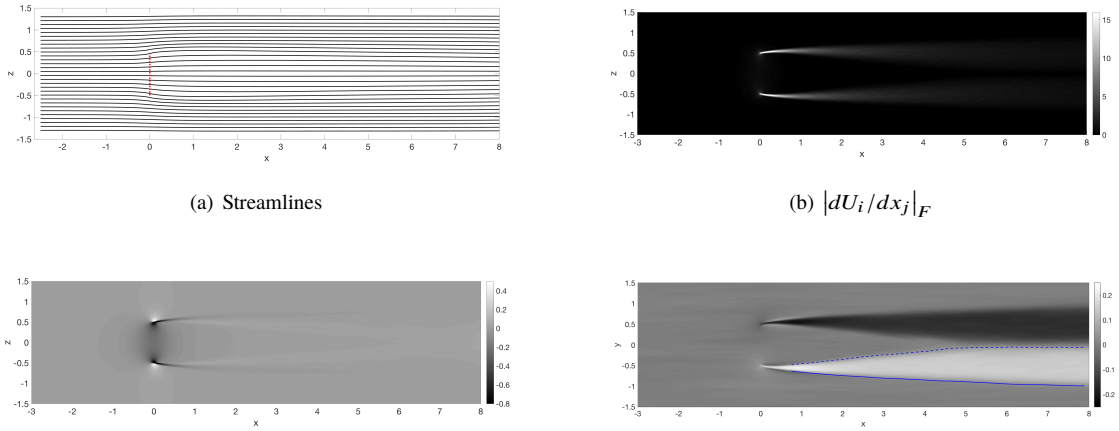

(a) Streamlines

(b) $\left|dU_i/dx_j\right|_F$

(c) dU/dx

(d) b_{13}

Fig. 3 Mean flow properties for Case 10 HIT inflow shown along the x-z plane. The blue lines in subfigure (d) indicate $|b_{13}| = 0.03$, a threshhold used to identify the wake shear layer turbulence.

The anisotropy tensor, $b_{ij} = R_{ij}/R_{kk} - \delta_{ij}/3$ will be used throughout this paper to characterize the anisotropy of the flow. By construction, the tensor is zero in regions of isotropic turbulence. When the flow is visualized on the xz plane the component b_{13} of the anisotropy tensor serves as a measure for the correlation between the axial and radial velocity components. This component for Case 10 HIT inflow is shown in Figure 3d. In order to characterize the shear layer thickness, which is synonymous to wake recovery in the present context, the non-dimensional measure for shear layer turbulence can be thresholded (to a value of 0.03 in the present study) to obtain the inner and outer radii of the region entrained by the shear layer. These two bounds are identified in blue in the contour plot shown in Figure 3d.

The inner and outer radius of the shear layer, along with its thickness is shown in Figure 4. The sensitivity of the wake recovery to the upstream turbulence intensity is quite evident. However, it is instructive to note that while Case 20 and Case 1 have approximately the same turbulence intensities at incidence, the shear layer grows substantially faster for the Case 20, which corresponds to HIT inflow with a larger integral length scale. This is also seen in the scaling (slope) of the inner core entrainment; the slope is a stronger function of the *integral length scale*, and a weak function of the *intensity* (or dissipation rate). This observation is revisited in Section 5 where the space-time POD analysis is used to show that the larger length scale incident turbulence creates an initial perturbation to the shear layer with a larger projection onto low Strouhal number (large wavelength) Kelvin-Helmholtz wavepackets, thereby increasing the growth rate of the shear layer.

III. Turbulence anisotropy and pressure decomposition

In this section, we will consider the large length scale, large dissipation rate incident HIT (Case 10) and characterize the Reynolds stress anisotropy of the AD wake turbulence using a multiscale decomposition. The non-zero components of the Reynolds stress anisotropy tensor along the xz plane are shown in Figure 5. The core flow shows an amplification of the axial component and a dampening of the other two components, due to axisymmetric expansion of the HIT that occurs at the actuator disk. The entrainment of this anisotropic (but primarily Gaussian) turbulence by the anisotropic shear layer (highly non-Gaussian; the axial and radial velocity components have high skewness) appears to be a complex phenomenon which manifests itself in terms of troughs and ridges in b_{11} (axial, Figure 5(a)) and b_{33} (radial, Figure 5(c)) components respectively. This restructuring of the flow can be better understood by using a 3-scale decomposition of the turbulence flow field variables.

An example instantaneous snapshot of the 3-scale decomposition of the axial velocity, u, is shown in Figure 6. Such a decomposition was obtained by successive filtering using a 5-pt. implicit *Padé* filter[33] which provides sufficient spectral sharpness while minimizing Gibbs oscillations at the thin shear layers. The anisotropy of the individual scales are shown in Figure 7. Comparing Figure 5(a) with Figures 7(a-c) and Figure 5(c) with Figures 7(d-f), it is clear that the troughs and ridges are primarily due to the restructuring of the large, highly anisotropic scales in the core as they get

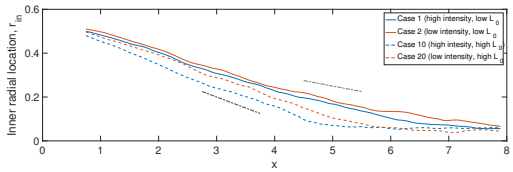

(a) Inner radius

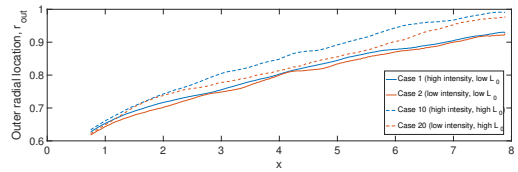

(b) Outer radius

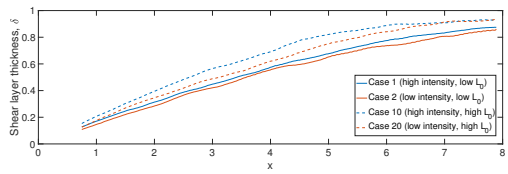

(c) Shear layer thickness

Fig. 4 Wake shear layer spread as a function of downstream distance

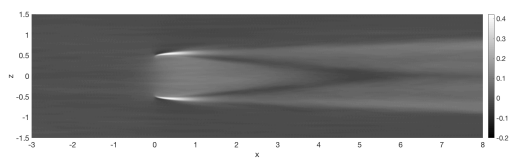

(a) b_{11}

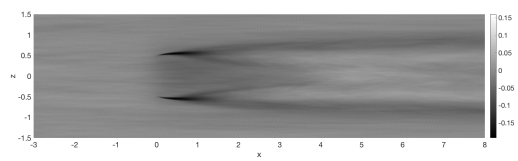

(b) b_{22}

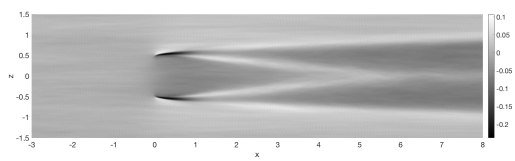

(c) b_{33}

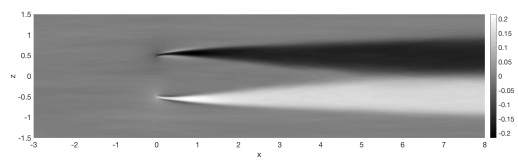

(d) b_{13}

Fig. 5 Reynolds stress anisotropy along the xz centerplane for the Case 10 inflow HIT

entrained by the shear layers. The y-z contour plots (Figures 7(g-l)) taken $0.5D$ downstream of the AD further illustrate that the bulk of the asymmetric expansion of the HIT ingested by the AD is felt by the large scales. This observation is consistent linear theory, which predicts lower distortion of small scales due to their faster decorrelation time scale compared to the travel time through the region of high axial gradient (see Figure 3c). The circular rings/halos seen in both scales B and C (Figures 7(h-i) and (k-l)) show that the dominant feature in the flow just 0.5D downstream of the AD is the shear layer turbulence, which is seen as a larger amplification of the axial component, along with much more aggressive suppression (compared to the expansion at the core) of the radial velocity component.

Next, we discuss the turbulent pressure characteristics in the flow. It is pertinent to decompose the computed pressure as a superposition of 4 different contributions. Since the flow being considered is incompressible and constant density, we can obtain the following 4 components for the computed pressure by solving 4 Poisson equations.

1) *True* pressure:

$$\partial_j \partial_j p_{\text{true}} = -\partial_j \partial_i u_i u_j$$

2) *SGS contribution* for an eddy viscosity closure:

$$\partial_j \partial_j \left(p_{\text{sgs}} + \frac{1}{3} \tau_{kk}^{\text{sgs}} \right) = -\partial_i \partial_j \tau_{ij}^{\text{d}}$$

3) *Fringe* contribution:

$$\partial_j \partial_j p_{\text{fringe}} = (u_j - u_j^{\text{targ}}) \partial_j g_{\text{fringe}}$$

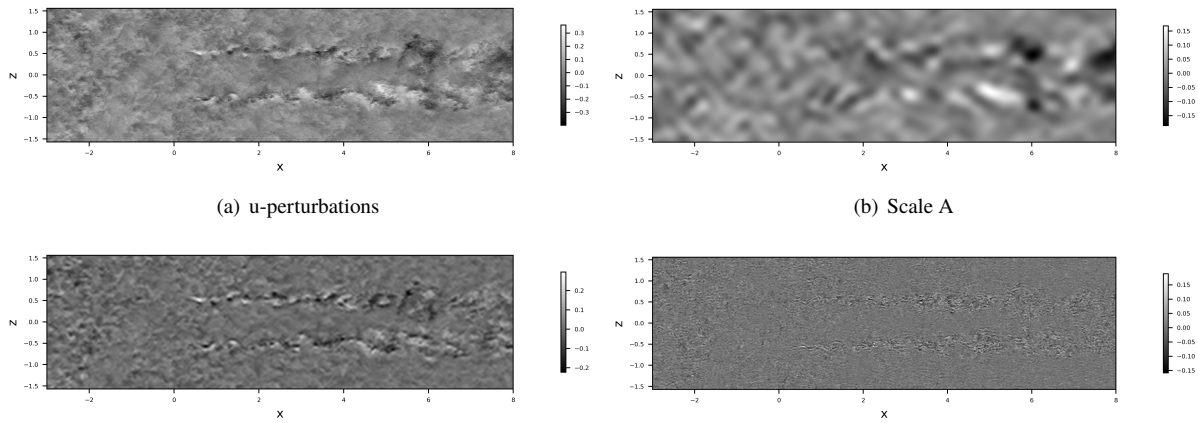

(a) u-perturbations

(b) Scale A

(c) Scale B

(d) Scale C

Fig. 6 Multiscale decomposition of the instantaneous velocity perturbations into 3 separate scales

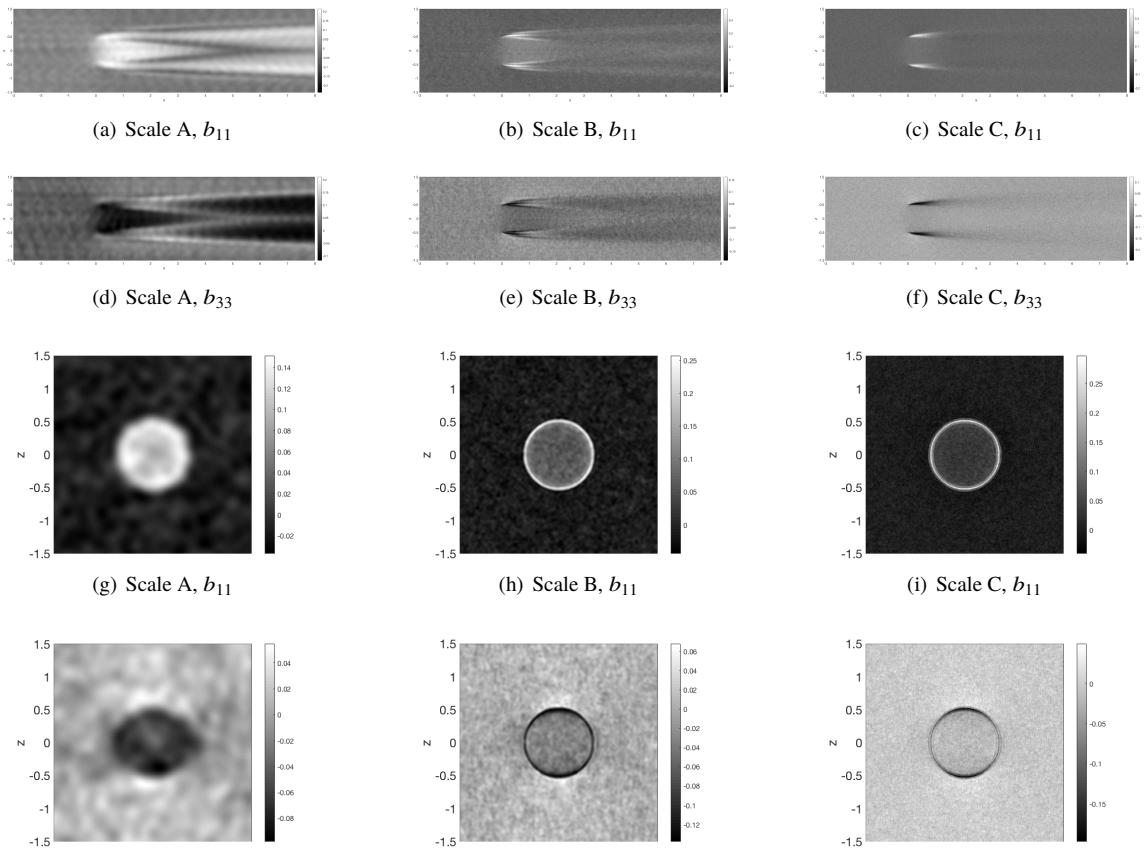

(a) Scale A, b_{11}

(b) Scale B, b_{11}

(c) Scale C, b_{11}

(d) Scale A, b_{33}

(e) Scale B, b_{33}

(f) Scale C, b_{33}

(g) Scale A, b_{11}

(h) Scale B, b_{11}

(i) Scale C, b_{11}

(j) Scale A, b_{33}

(k) Scale B, b_{33}

(l) Scale C, b_{33}

Fig. 7 Reynolds stress anisotropy components, b_{11} and b_{33} at the three scales. Subfigures (g)-(l) show the anisotropy tensor components on the yz planes taken approximately $0.5D$ downstream of the AD.

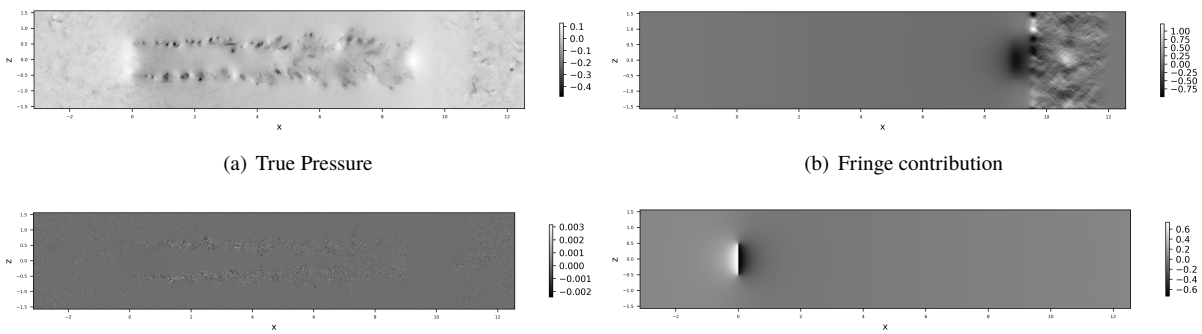

(a) True Pressure

(b) Fringe contribution

(c) SGS model contribution

(d) AD contribution

Fig. 8 Computed pressure decomposed into 4 contributions

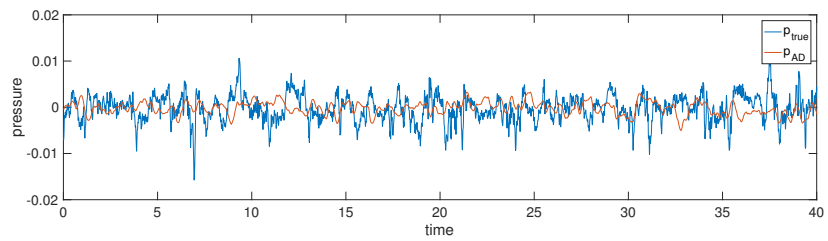

(a) Fluctuating signals

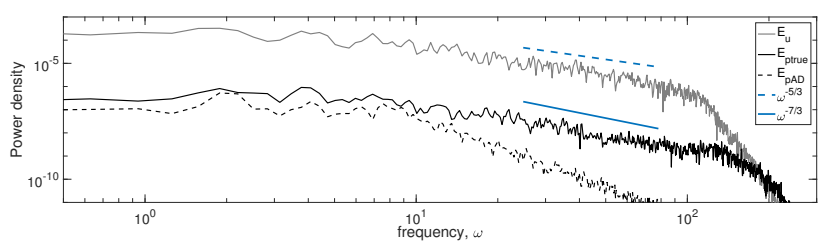

(b) Frequency spectrum

Fig. 9 Pressure measured at a probe located 0.5D downstream along the centerline of the AD

4) Actuator disk contribution:

$$\partial_j \partial_j p_{\mathrm{AD}} = \partial_j f_j^{\mathrm{AD}}$$

The xz contours of instantaneous snapshots of the four contributions to pressure are shown in Figure 8. The SGS contribution (Figure 8(c)) is approximately 2 orders of magnitude smaller than the other contributions, which suggests that the numerical resolution is sufficiently high. This decomposition also shows the region of the domain contaminated by the fringe/sponge layer being used (Figure 8(b)) and note that a substantial portion of the simulated domain appears to be available to study the wake growth downstream of the AD. The presence of the actuator disk creates a pressure dipole (Figure 8(d)), with fluctuations resulting due to the low pass filtering of the incident HIT caused by the AD. This is also evident from Figure 9(a), which shows the signal measured by a probe located $0.5D$ downstream along the centerline of the AD. Figure 9 also shows that the *true* pressure along with the axial velocity component measured at this location shows the expected $-7/3$rd and $-5/3$rd frequency scaling respectively, and that the low frequency contribution to the fluctuating pressure by the AD force is not negligible compared to the true pressure.

It is instructive to further decompose the fluctuating part of the *true* pressure fields into components that have colloquially been referred to as *rapid* (associated with the mean flow gradient) and *slow* (associated with correlations between fluctuating velocity gradients) contributions. Such a decomposition applied to the true pressure fields (in Figure 8a) is shown in Figure 10, where the true pressure is decomposed into the mean (time averaged) components, and

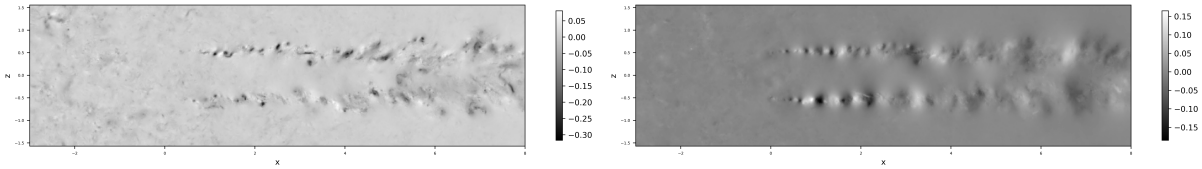

(a) Slow component

(b) Rapid component

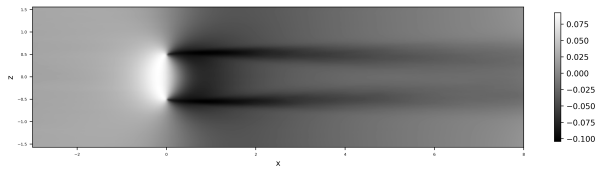

(c) Mean (time averaged) component

Fig. 10 *True* pressure further decomposed into 3 components

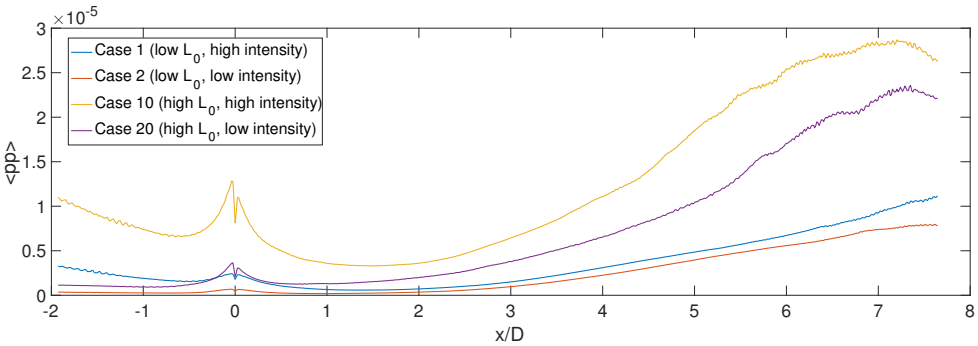

(a) pressure variance, through the centerline (z=0D)

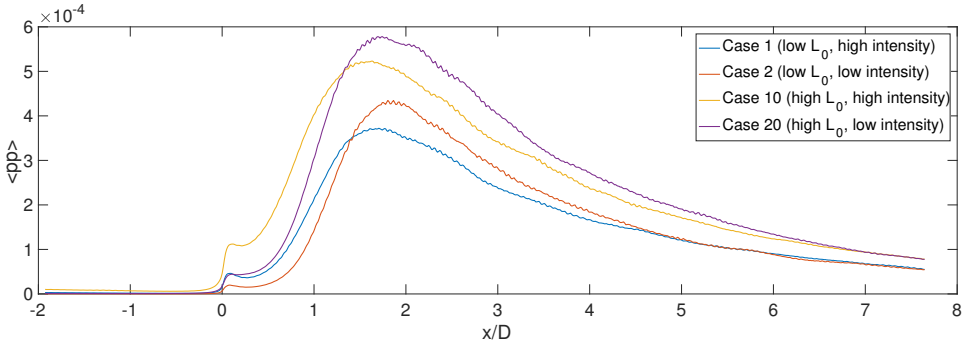

(b) pressure variance, through the shear layer (z=0.5D)

Fig. 11 Pressure fluctuation variance ($< pp > /U_0^4$) as a function of x for the different inflow cases.

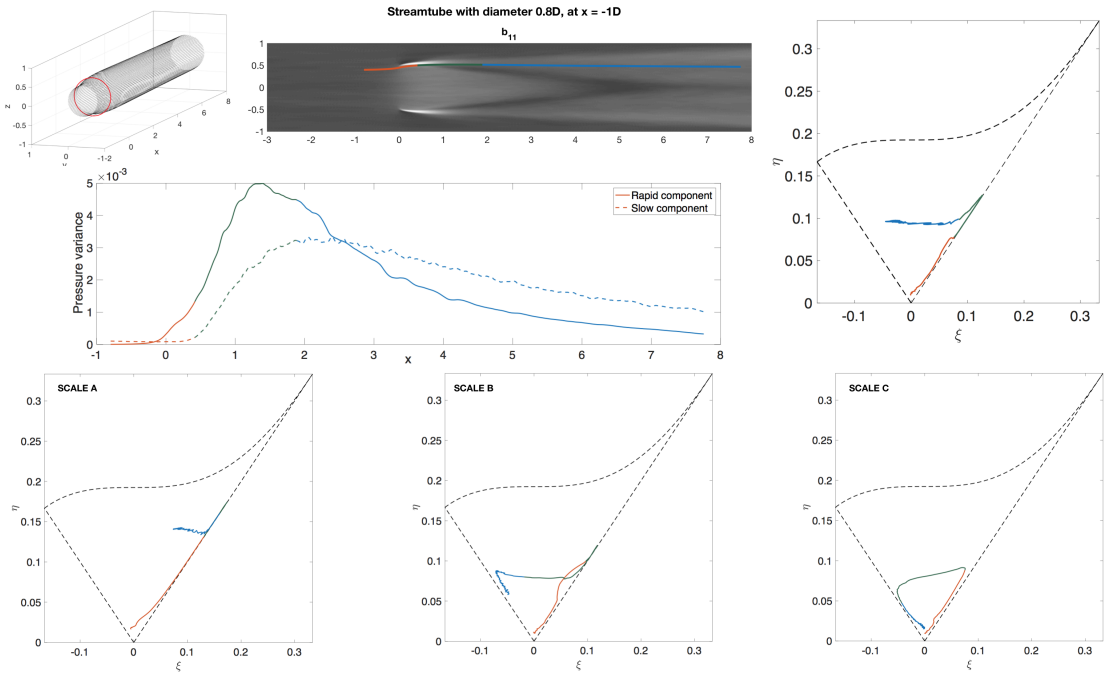

Fig. 12 Azimuthally averaged, multi-scale Reynolds stress anisotropy invariants plotted in the Lumley triangle, along with rapid and slow pressure variances plotted along an expanding streamtube of diameter 0.8D (when 1D upstream of the AD).

the rapid and slow components.

With these decompositions applied to pressure, it is now possible to interpret the turbulent pressure variance profiles plotted in Figure 11. Subfigure (a) shows the pressure variance for the different cases along the centerline/axis of the actuator disk. The first feature, which is a jump around the actuator disk location, is due to the increase in a) the fluctuating component of the actuator disk contribution (dipole) to the pressure, and b) rise in both the rapid and the slow components of pressure due to the axisymmetric expansion of the HIT. Note that this increase in the rapid component does not overwhelm the slow component (there doesn't appear to be any evidence of *rapid* expansion), which is also seen in the instantaneous snapshots for the rapid and slow pressure components. The increase in the actuator disk contribution to pressure fluctuations shows the expected sensitivity to the integral length scale of the incident turbulence, and also to its intensity. The second feature, a more gradual rise in pressure variance, is a consequence of the shear layer penetrating (or entraining) the core region.

More interesting observations are possible when we consider the turbulence pressure variance through the shear layer (edge of the actuator disk), Figure 11(b). The first feature observed is a sudden rise in the pressure fluctuations, which appear to plateau through approximately $0.5D$ downstream of the AD. This region is characterized primarily by a large jump in the fluctuating pressure dipole, and also a large, sudden increase in the rapid component of the fluctuating true pressure, while the slow component is relatively unaffected (this is seen in the pressure variances shown in Figure 12). Further downstream, the AD contribution to pressure decays as the rapid component continues to rise, eventually reaching peak intensity approximately 1.4D downstream of the AD. The slow component increases gradually as a function of the downstream distance and becomes comparable to the rapid pressure 2-3D downstream, and both components gradually drop off as the shear layer entrains the entire core region along with the surrounding ambient HIT coflow.

The pressure variance through the shear layer appears to be strongly sensitive to integral length scale of the upstream turbulence. As shown later in section IV this large variance is almost entirely due to the increased energy in the low-Strouhal number (low frequency, high wavelength) Kelvin-Helmholtz wavepackets when the initial perturbation is provided by larger length scale HIT. Figure 11(b) also shows that the peak pressure fluctuation variance for the cases with lower dissipation rate (lower intensity) HIT inflow (Case 2 and 20) is higher than that for the cases with higher dissipation rate (Cases 1 and 10). This feature in the variance profiles will again be addressed in Section IV, where we

argue that this peak is due to an intermediate range of higher Strouhal number KH wavepackets (St between 0.2 to 0.5) where the exponentially growing wavepackets reach a saturation further downstream, and also have higher modal energies for the cases with low turbulent intensity inflow (Cases 2 and 20 compared with Cases 1 and 10 respectively).

It is now possible to describe the overall flow structure by analyzing the statistics along streamtubes of different radii that begin upstream of the AD. Figure 12 depicts the azimuthally averaged statistics for a streamtube of radius $0.4D$ beginning approximately $1D$ downstream of the actuator disk. The trajectory is split into three prominant features: a) the axisymmetric expansion as the streamtube is ingested by the actuator disk (colored in red), b) passage through the region where the anisotropic core turbulence is entrained by the shear layer (colored in green), and c) passage through the wake shear layer (colored in blue). The overall flow structure quantified using Reynolds stress anisotropy invariant within the Lumley triangle is quite complex. However, once decomposed within separate scales, the interpretation of the interaction between the HIT and the AD wake becomes easier. The first interaction of the incident HIT with the AD is characterized by an expansion where all three scales are dominated by an amplified axial component (1-component limit), however the largest scales are most strained. Further downstream, both scales, B and C, show evidence of transitioning from strongly 1-component towards two dominant components (axial and azimuthal), as is expected in shear turbulence. However, the largest scales appear to undergo more complex behavior. Eventually, as the streamtube enters the shear layers, the largest scales (Scale A) retain the 2-component anisotropy expected in shear layer turbulence. However, it is interesting to note that the smallest scales (Scale C) appear to tend towards isotropy (which is expected as the length scale of the shear layer increases), along the 2-component limit.

IV. Modal decomposition and sensitivity of shear layer growth to inflow turbulence

Modal decomposition methods such as Proper Orthogonal Decomposition (POD) and Dynamic Mode Decomposition (DMD) have received increased attention in the wind energy research community recently. POD has been used to identify dominant flow structures and the associated kinetic energy entrainment (see VerHulst & Meneveau [18]) and to quantify large scale flow anisotropy (see Hamilton et al. [34]). However, as noted in recent work by Towne et. al. (2017)[29] such a *space-only* modal decomposition leads to identification of spatially orthogonal modes with expansion coefficients that have random time dependence. As such these modes lack information regarding any space-time coherence in the flow. An extension of DMD (which captures space-time coherence), termed Input-Output DMD (IODMD) (see Annoni et al. [35]) has recently been proposed as a relevant reduced order modeling strategy to allow for testing of unsteady wind farm control strategies at lower computational cost than LES.

Since the present work focuses on a temporally stationary flow where the primary interest is in characterizing the sensitivity of the shear layer growth to the intensity and length scale of the incident HIT, we are interested in finding the optimal DMD modes for a given temporal frequency. Towne et al. (2017) [29] show that Lumley's (1970)[28] original POD formulation, herein referred to as SPOD *identifies the DMD modes that have been optimally averaged to provide the best possible representation of the second order space-time statistics* for a temporally stationary flow. The underlying idea behind SPOD is to decompose the temporal Fourier transform (which encapsulates two-point temporal correlations) of the solution $q(\boldsymbol{x}, t)$ as a superposition of spatially orthogonal modes:

$$\hat{q}(\boldsymbol{x}, f) = \sum_{j=1}^{\infty} a_j(f)\psi_j(\boldsymbol{x}, f), \tag{1}$$

where the energy in each mode, $\psi_j(\boldsymbol{x}, f)$, is given as the expected value of the uncorrelated coefficients, $\lambda_i(f)\delta_{ij} = E\left\{a_i(f)a_j^{\star}(f)\right\}$. The reader is referred to Towne et al. (2017)[29] for further details regarding SPOD including the algorithm used to compute the modes presented in this paper.

The SPOD for the simulation with Case 10 HIT inflow is shown in Figure 13. The subfigures (a) and (c) show the modal energies for the 30 most energetic modes as a function of Strouhal number ($St = fD/U_0$) computed using two different energy norms (turbulent kinetic energy in (c), and turbulent pressure variance in (a)). Both results show that the energies decay at increasing frequencies (with the expected scaling of $-7/3$ and $-5/3$ for total modal energy at a given frequency). Subfigures (b) and (d) show the relative contribution of each mode to the energy at a certain frequency. The pressure variance error norm-minimizing decomposition clearly suggests that the entire problem has a low rank in terms of the SPOD modes, especially at low frequencies; about 90% of the total energy at $St = 0.12$ can be captured using the first 12 modes. However, when we consider the TKE error norm-minimizing decomposition at $St = 0.12$, the first 12 modes combine to produce less than 50% of the total energy. This is not surprising, since the pressure variance averaged through the entire domain is primarily due to the increase in pressure fluctuations in the shear layer; the same is not true

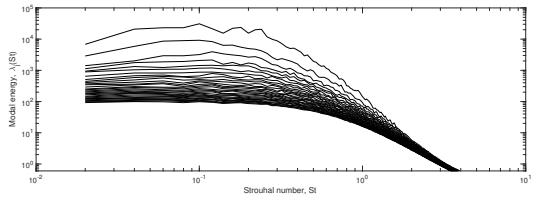

(a) Modal energies using the turbulent pressure variance norm

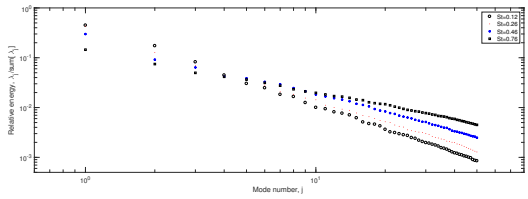

(b) Relative modal energies at 4 different frequencies using the turbulent pressure variance norm

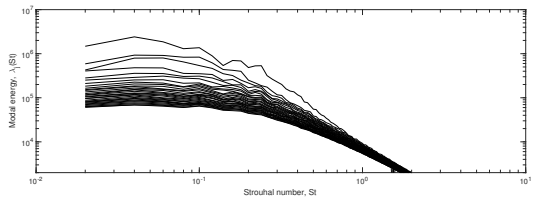

(c) Modal energies using the turbulent kinetic energy norm

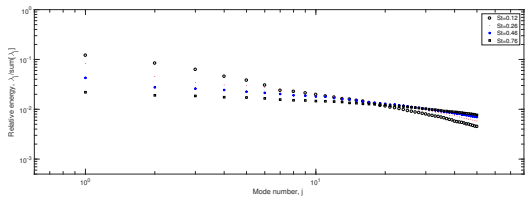

(d) Relative modal energies at 4 different frequencies using the turbulent kinetic energy norm

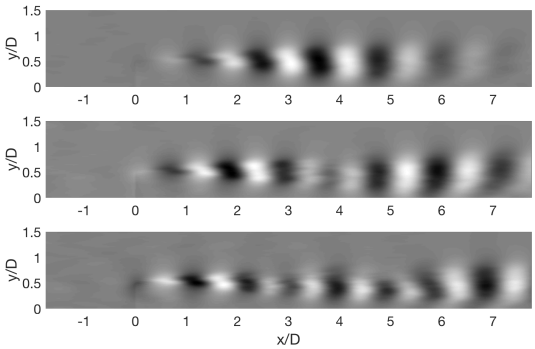

(e) First 3 pressure modes at St=0.12

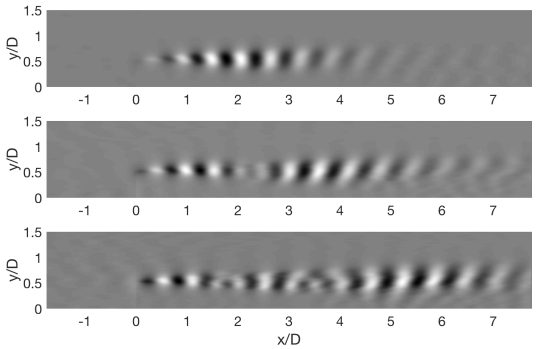

(f) First 3 pressure modes at St=0.26

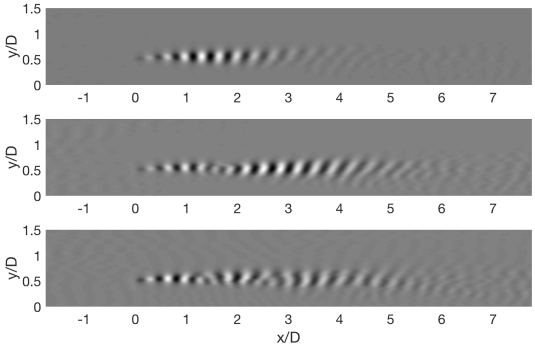

(g) First 3 pressure modes at St=0.46

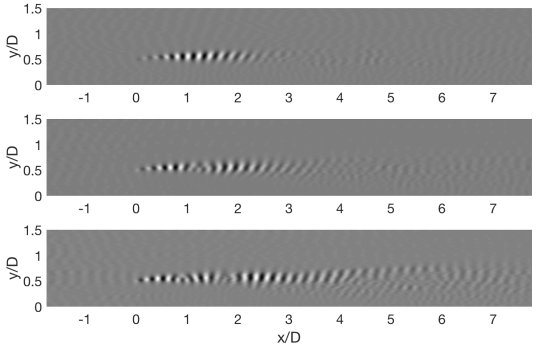

(h) First 3 pressure modes at St=0.76

Fig. 13 Spectral Proper Orthogonal Decomposition (SPOD) of the simulation data with Case 10 HIT inflow

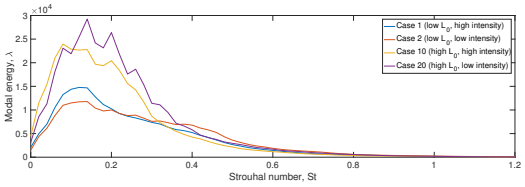

(a) Modal energies for the 1st mode as a function of frequency

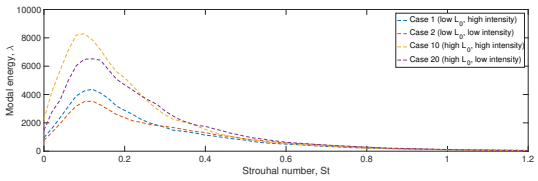

(b) Modal energies for the 2nd mode as a function of frequency

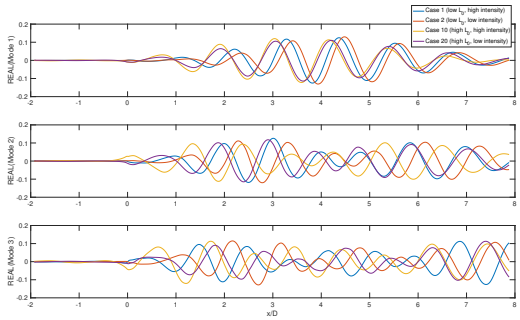

(c) Real part of the first 3 modes (z=0.5D) St=0.12

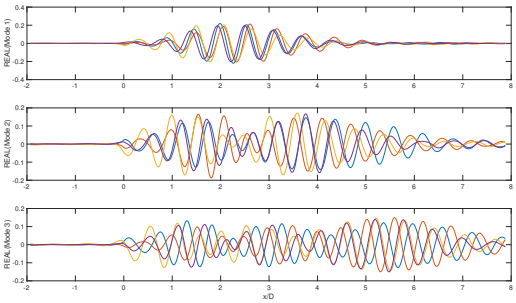

(d) Real part of the first 3 modes (z=0.5D) St=0.26

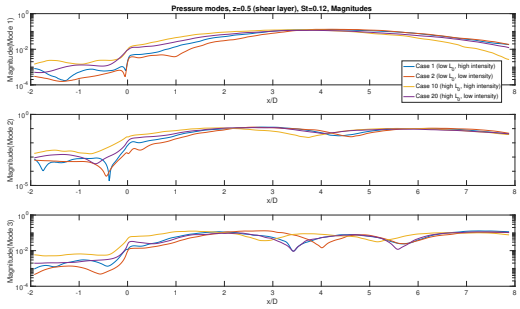

(e) Magnitude of the first 3 modes (z=0.5D) St=0.12

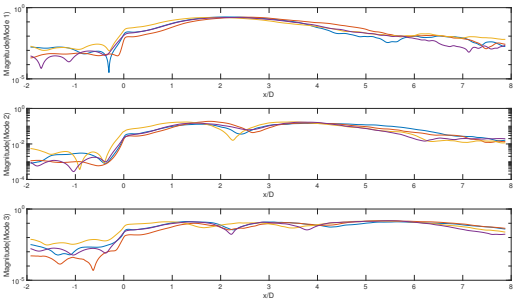

(f) Magnitude of the first 3 modes (z=0.5D) St=0.26

Fig. 14 Comparison between the model energies and mode shapes for the Kelvin Helmholtz wavepackets at low Strouhal numbers for the 4 different inflow HIT cases simulated. The model decomposition was performed using the pressure variance norm.

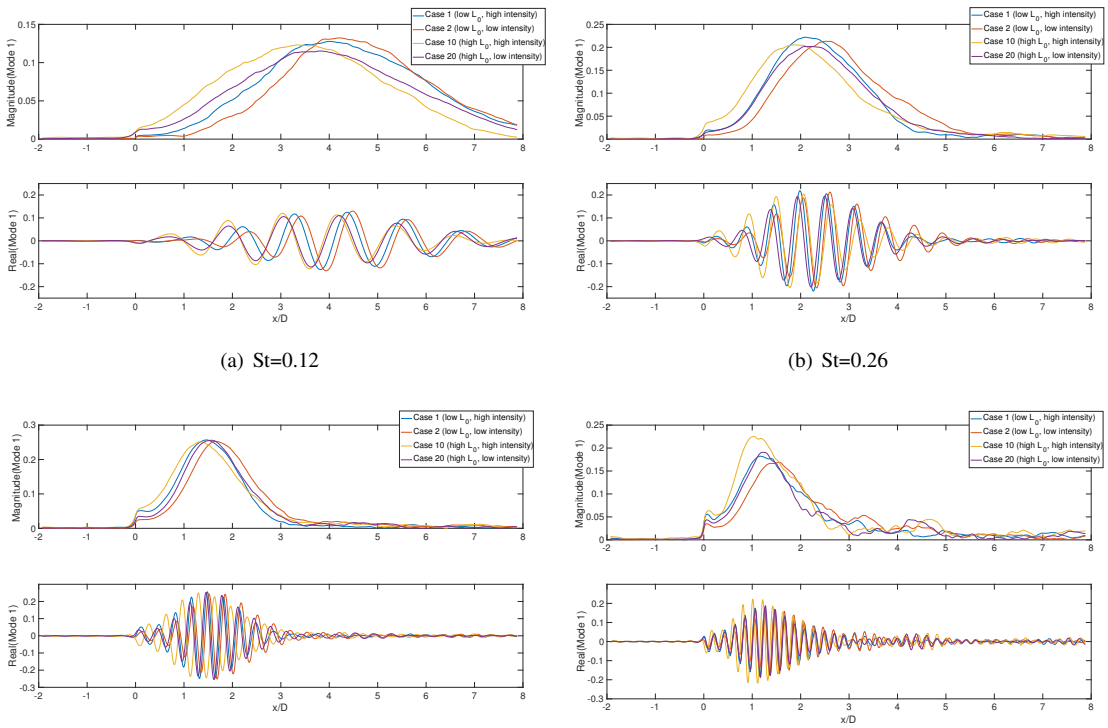

(a) St=0.12

(b) St=0.26

(c) St=0.46

(d) St=0.76

Fig. 15 The first mode shape (along z=0.5D) as a function of downstream distance for 4 different Strouhal numbers.

for TKE since a substantial portion of TKE is present in the incident HIT, the core flow, and the exterior HIT co-flow. Subfigures (e) - (h) show the first 3 pressure modes (real part of $\psi_j(\boldsymbol{x}, f)$) at 4 different Strouhal numbers. The first mode at each frequency shows the primary KH wavepackets where the energy grows exponentially downstream from the AD and eventually saturates, roughly 2-3 D downstream from the AD, eventually decaying as the shear layer engulfs the entire core to create a fully turbulent wake. The higher order modes at each frequency represent the variability in the KH vortices seen in the instantaneous pressure fields.

The comparisons between the different inflow cases are shown in Figure 14, where both, the real part and the magnitude of the KH pressure wavepackets, are shown as functions of downstream distance. The subfigures (a) and (b) which display the modal energies for the first two modes as a function of Strouhal number show that the larger integral length scale in upstream turbulence is seen as a larger projection on low Strouhal number (large wavelength) KH wavepackets, which corresponds to the bulk of the entrainment/growth of the shear layers. Figure 15 shows the replotting of Mode 1 using linear scaling in y to illustrate that for a certain range of Strouhal numbers (see subfigures b and c) the lower intensity inflow HIT results in the first mode saturating at a further downstream distance. It is also evident in the modal energies for the first mode (see Figure 14a) that, at these intermediate Strouhal numbers, the first mode is more energetic for the low intensity (Cases 2 and 20) inflow cases (compared to Cases 1 and 10 respectively). It is pertinent to note this is consistently seen as an increased peak turbulent pressure variance in the shear layers, as was also noted in Figure 11(b).

V. Conclusion

In this paper we present results for highly resolved LES to study the deformation of small integral length scale Homogeneous Isotropic Turbulence (HIT) by a constant thrust coefficient actuator disk. By varying two properties of the inflow HIT, namely the integral length scale, and the dissipation rate, we are able to distinguish between the varying effects of the parameters on the wake shear layer growth and, effectively, the wake recovery process. The turbulent wake

structure is analyzed in detail using a 3-scale decomposition of the flow field.

Using a space-time modal decomposition, we demonstrate that the primary parameter that influences the shear layer growth (and hence the wake recovery) is the *integral length scale* of the incident turbulence, as opposed to its *intensity*. The influence of the intensity (strictly speaking, the *dissipation rate*) is observed in terms of an intermediate range of frequencies at which the most energetic KH wavepackets saturate (and subsequently decay) at distances further downstream and as such attain larger peak amplitudes, thereby creating a larger peak turbulent pressure variance in the wake shear layers. The shear layer growth is primarily due to the low frequency KH wavepackets, which are strongly influenced by the integral length scale of the incident turbulence.

It is important to note that the while the use of a turbulent pressure variance error norm in the SPOD suggests a low-rank nature of the overall flow, the turbulence kinetic energy norm does not confirm this behavior. This is likely due to the multiscale aspect of the HIT-shear layer interaction with a non-negligible amount of the total turbulent kinetic energy being contributed by the axisymmetrically expanded core and the HIT co-flow.

It is also pertinent to note that the axisymmetric expansion of the HIT does not appear to be within the *rapid distortion* limit, with neither the slow component nor the rapid component of pressure dominating. The only region of the flow where the distortion does appear to occur at a rapid time scale is the region near the actuator disk boundaries (see the streamtube shown in Figure 12, and also Figure 3b). However, the mean flow in this region is far from irrotational, thereby restricting the use of Rapid Distortion Theory (RDT) in the classical sense.

Acknowledgments

The simulations were performed on *Peregrine* supercomputer using computer time that was graciously provided by National Renewable Energy Lab (NREL). The help provided by Ganesh Vijaykumar (Postdoc, NREL), and Matt Churchfield (Senior Engineer, NREL) regarding *Peregrine* usage and access to the allocation, is gratefully acknowledged. This research was financially supported via a seed grant provided by the Tomkat Center for Sustainable Energy at Stanford University.

References

[1] Bontempo, R., and Manna, M., "Solution of the non-uniform heavily loaded ducted actuator-disk," *Journal of Fluid Mechanics*, Vol. 728, 2013, pp. 163–195.

[2] Bontempo, R., Cardone, M., Manna, M., and Vorraro, G., "Ducted propeller flow analysis by means of a generalized actuator disk model," *Energy Procedia*, Vol. 45, 2014, pp. 1107–1115.

[3] Chuiton, F. L., "Actuator disc modelling for helicopter rotors," *Aerospace Science and Technology*, Vol. 8, 2004, pp. 285–297.

[4] Mentey, J., "Time dependent actuator disk model for a helicopter rotor in hover," Master's thesis, Pennsylvania State University, 2012.

[5] Mikkelsen, R., "Actuator Disk Methods Applied to Wind Turbines," Ph.D. thesis, Technical University of Denmark, 2003.

[6] Wu, Y.-T., and Porté-Agel, "Large-Eddy Simulation of Wind-Turbine Wakes: Evaluation of Turbine Parameterizations," *Boundary Layer Meteorology*, Vol. 138, No. 13, 2011, pp. 345–366.

[7] Chamorro, L. P., and Porté-Agel, F., "A wind-tunnel investigation of wind-turbine wakes: boundary-layer turbulence effects," *Boundary-layer meteorology*, Vol. 132, No. 1, 2009, pp. 129–149.

[8] Barthelmie, R. J., Hansen, K., Frandsen, S. T., Rathmann, O., Schepers, J., Schlez, W., Phillips, J., Rados, K., Zervos, A., Politis, E., et al., "Modelling and measuring flow and wind turbine wakes in large wind farms offshore," *Wind Energy*, Vol. 12, No. 5, 2009, pp. 431–444.

[9] Ainslie, J. F., "Calculating the flowfield in the wake of wind turbines," *Journal of Wind Engineering and Industrial Aerodynamics*, Vol. 27, No. 1-3, 1988, pp. 213–224.

[10] Keck, R.-E., Maré, M., Churchfield, M. J., Lee, S., Larsen, G., and Madsen, H. A., "Two improvements to the dynamic wake meandering model: including the effects of atmospheric shear on wake turbulence and incorporating turbulence build-up in a row of wind turbines," *Wind Energy*, Vol. 18, No. 1, 2015, pp. 111–132.

[11] Jensen, N. O., *A note on wind generator interaction*, 1983.

[12] Frandsen, S., "On the wind speed reduction in the center of large clusters of wind turbines," *Journal of Wind Engineering and Industrial Aerodynamics*, Vol. 39, No. 1-3, 1992, pp. 251–265.

[13] Bastankhah, M., and Porté-Agel, F., "A new analytical model for wind-turbine wakes," *Renewable Energy*, Vol. 70, 2014, pp. 116–123.

[14] Peña, A., and Rathmann, O., "Atmospheric stability-dependent infinite wind-farm models and the wake-decay coefficient," *Wind Energy*, Vol. 17, No. 8, 2014, pp. 1269–1285.

[15] Stevens, R. J., Gayme, D. F., and Meneveau, C., "Effects of turbine spacing on the power output of extended wind-farms," *Wind Energy*, Vol. 19, No. 2, 2016, pp. 359–370.

[16] Churchfield, M. J., Lee, S., Michalakes, J., and Moriarty, P. J., "A numerical study of the effects of atmospheric and wake turbulence on wind turbine dynamics," *Journal of turbulence*, , No. 13, 2012, p. N14.

[17] Calaf, M., Meneveau, C., and Meyers, J., "Large eddy simulation study of fully developed wind-turbine array boundary layers," *Physics of fluids*, Vol. 22, No. 1, 2010, p. 015110.

[18] VerHulst, C., and Meneveau, C., "Large eddy simulation study of the kinetic energy entrainment by energetic turbulent flow structures in large wind farms," *Physics of Fluids*, Vol. 26, No. 2, 2014, p. 025113.

[19] Quarton, D., and Ainslie, J., "Turbulence in wind turbine wakes," *Wind Engineering*, 1990, pp. 15–23.

[20] Crespo, A., Herna, J., et al., "Turbulence characteristics in wind-turbine wakes," *Journal of wind engineering and industrial aerodynamics*, Vol. 61, No. 1, 1996, pp. 71–85.

[21] Xie, S., and Archer, C., "Self-similarity and turbulence characteristics of wind turbine wakes via large-eddy simulation," *Wind Energy*, Vol. 18, No. 10, 2015, pp. 1815–1838.

[22] Abkar, M., and Porté-Agel, F., "Influence of atmospheric stability on wind-turbine wakes: A large-eddy simulation study," *Physics of fluids*, Vol. 27, 2015, p. 035104.

[23] Mann, J., "The spatial structure of neutral atmospheric surface-layer turbulence," *Journal of fluid mechanics*, Vol. 273, 1994, pp. 141–168.

[24] Veers, P. S., *Modeling stochastic wind loads on vertical axis wind turbines*, Sandia National Laboratories, 1984.

[25] Jonkman, B. J., and Buhl Jr, M. L., "TurbSim user's guide," *National Renewable Energy Laboratory*, 2009.

[26] Ghate, A. S., and Lele, S. K., "Subfilter-scale enrichment of planetary boundary layer large eddy simulation using discrete Fourier–Gabor modes," *Journal of Fluid Mechanics*, Vol. 819, 2017, pp. 494–539.

[27] Martinéz Tossas, L., "Large Eddy Simulations and Theoretical Analysis of Wind Turbine Aerodynamics Using an Actuator Line Model," Ph.D. thesis, Johns Hopkins University, 5 2017.

[28] Lumley, J. L., *Stochastic tools in turbulence*, Academic Press, 1970.

[29] Towne, A., Schmidt, O. T., and Colonius, T., "Spectral proper orthogonal decomposition and its relationship to dynamic mode decomposition and resolvent analysis," *arXiv preprint arXiv:1708.04393*, 2017.

[30] Nordström, J., Nordin, N., and Henningson, D., "The fringe region technique and the Fourier method used in the direct numerical simulation of spatially evolving viscous flows," *SIAM Journal on Scientific Computing*, Vol. 20, No. 4, 1999, pp. 1365–1393.

[31] Nicoud, F., Toda, H. B., Cabrit, O., Bose, S., and Lee, J., "Using singular values to build a subgrid-scale model for large eddy simulations," *Physics of Fluids*, Vol. 23, No. 8, 2011, p. 085106.

[32] Gottlieb, S., Shu, C.-W., and Tadmor, E., "Strong stability-preserving high-order time discretization methods," *SIAM review*, Vol. 43, No. 1, 2001, pp. 89–112.

[33] Spyropoulos, E. T., and Blaisdell, G. A., "Evaluation of the dynamic model for simulations of compressible decaying isotropic turbulence," *AIAA journal*, Vol. 34, No. 5, 1996, pp. 990–998.

[34] Hamilton, N., Tutkun, M., and Cal, R. B., "Anisotropic character of low-order turbulent flow descriptions through the proper orthogonal decomposition," *Physical Review Fluids*, Vol. 2, No. 1, 2017, p. 014601.

[35] Annoni, J., Gebraad, P., and Seiler, P., "Wind farm flow modeling using input-output dynamic mode decomposition," *American Control Conference (ACC)*, 2016.